energies

MDPI

Article

Assessment against Experiments of Devolatilization and Char Burnout Models for the Simulation of an Aerodynamically Staged Swirled Low-NO_x Pulverized Coal Burner

Marco Torresi [1,*], Francesco Fornarelli [1,*], Bernardo Fortunato [1], Sergio Mario Camporeale [1] and Alessandro Saponaro [2]

[1] Department of Mechanics, Mathematics and Management (DMMM), Polytechnic of Bari, via Orabona 4, 70125 Bari, Italy; bernardo.fortunato@poliba.it (B.F.); sergio.camporeale@poliba.it (S.M.C.)

[2] Combustion and Environment Research Centre (CCA)—Ansaldo Caldaie, via Vicinale Milano, km 1.600, 70023 Gioia del Colle, Italy; alessandro.saponaro@ansaldoboiler.it

* Correspondence: marco.torresi@poliba.it (M.T.); francesco.fornarelli@poliba.it (F.F.); Tel.: +39-080-596-3577 (M.T.)

Academic Editor: Mehrdad Massoudi
Received: 6 December 2016; Accepted: 30 December 2016; Published: 7 January 2017

Abstract: In the next few years, even though there will be a continuous growth of renewables and a loss of the share of fossil fuel, energy production will still be strongly dependent on fossil fuels. It is expected that coal will continue to play an important role as a primary energy source in the next few decades due to its lower cost and higher availability with respect to other fossil fuels. However, in order to improve the sustainability of energy production from fossil fuels, in terms of pollutant emissions and energy efficiency, the development of advanced investigation tools is crucial. In particular, computational fluid dynamics (CFD) simulations are needed in order to support the design process of low emission burners. Even if in the literature several combustion models can be found, the assessment of their performance against detailed experimental measurements on full-scale pulverized coal burners is lacking. In this paper, the numerical simulation of a full-scale low-NO_x, aerodynamically-staged, pulverized coal burner for electric utilities tested in the 48 MW_{th} plant at the Combustion Environment Research Centre (CCA - Centro Combustione e Ambiente) of Ansaldo Caldaie S.p.A. in Gioia del Colle (Italy) is presented. In particular, this paper is focused on both devolatilization and char burnout models. The parameters of each model have been set according to the coal characteristics without any tuning based on the experimental data. Thanks to a detailed description of the complex geometry of the actual industrial burner and, in particular, of the pulverized coal inlet distribution (considering the entire primary air duct, in order to avoid any unrealistic assumption), a correct selection of both devolatilization and char burnout models and a selection of suited parameters for the NO_x modeling, accurate results have been obtained in terms of NO_x formation. Since the model parameters have been evaluated a priori, the numerical approach proposed here could be suitable to be applied as a performance prediction tool in the design of pulverized coal burners.

Keywords: computational fluid dynamics (CFD); pollutant emissions; pulverized coal combustion; industrial burner; devolatilization; char burnout; NO_x formation

1. Introduction

Recent statistics highlight that energy production will still be strongly fossil fuel dependent [1,2]. Over 90% of energy-related emissions are composed of CO_2 from fossil-fuel combustion. Even in

the optimistic scenario of a continuous growth of renewable energy with respect to fossil fuels, hydrocarbons will still be the dominant source of energy in 2035 with a share of 80%, compared to 86% in 2014 [3]. In particular, the oil share will continue to decline (from 32% to 29%), however keeping its leading position, together with coal (from 30% to 25%), which will be surpassed by natural gas (from 24% to 26%) [3]. However, the concern about pollutant emissions from coal promotes an efficiency improvement of the entire energy production technology. The optimization of the heat transfer in non-reacting parts [4–6] and the integration of renewable energy in conventional energy systems [7] represent just a few examples that indirectly reduce both the coal demand and the CO_2 emissions, for which computational fluid dynamics (CFD) has a key role. However, further developments are required to design low emission pulverized coal burners, characterized by low or negligible NO_x emissions and ashes with a very low carbon content. Several approaches have been developed in order to reduce the pollutant emissions in industrial furnaces: for instance, the introduction of the moderate and intense low oxygen dilution (MILD) technology in pulverized coal combustion to reduce the NO_x emissions [8,9]; the pulverized coal oxy-fuel combustion, with CO_2 capture from flue gas [10–12]; the combustion of syngas derived from waste biomass [13–15]; the co-firing of biomass and coal [16–18]. The research activities in this field are strictly dependent on a good understanding of the coal combustion processes in industrial applications, even though data concerning coal combustion are mostly obtained in laboratory-scale experiments, operating far from the actual industrial conditions [19]. Since there are few experimental measurements in industrial furnaces [19,20] and laboratory tests on full-scale burners are not easily practicable, numerical simulations can be used, being a common aid in order to investigate multiphase and combustion problems in a wide range of physical and engineering applications. In particular, the combustion of pulverized coal within combustion chambers has been studied numerically, due to the recent interest in this type of combustion technology. Yin and Yan [21] make a review of the modeling approach to pulverized coal combustion with an overview on physical fundamentals and technological issues. Rebola and Azevedo [22], Asotani et al. [23] highlight the influence of the operating conditions on the performance of the burner by means of CFD. Tan et al. [24] analyze the optimal pulverized coal concentration with respect to the flame temperatures and pollutants emissions (NO_x and fly ash). The pulverized coal combustion involves several aspects that need to be taken into account in the mathematical modeling of the problem. Recently, McConnell et al. [25], McConnell and Sutherland [26] and Goshayeshi and Sutherland [27] performed numerical simulations to investigate the combustion of a single coal particle. Their work confirms that the particle characteristics, the devolatilization and char burnout models are crucial in the prediction of combustion performance. The chemical species concentrations in the combustion process [28–30] and the temperature distribution [31–34] within the combustion chamber are the key features that a numerical model is able to describe in detail. Commonly, the two-phase flow, with the solid phase dispersed in the continuous phase, is numerically solved by means of an Eulerian-Lagrangian approach with one- or two-way coupling between the two phases. Inter alia, large eddy simulation (LES) analysis coupled with a particle Lagrangian model gives a high level of detail, but also requires a high computational time [35,36]. Furthermore, particular care should be taken in modeling the interaction of unresolved sub-grid LES scales with the dispersed phase [37]. On the other hand, the Reynolds Averaged Navier Stokes (RANS) approach with an adequate turbulence model provides a consistent solution of the mean flow field without the excessive computational effort of an LES approach [38]: the realizable k-ϵ model achieves good results in predicting swirling combustion flows [39,40]. The recent work of Saha et al. [41] confirms the reliability of the RANS approach in the case of pulverized coal MILD combustion. In order to reach consistent quantitative results, accurate experimental data represent a benchmark to validate the numerical codes and to be confident of the reliability of the numerical results (e.g., [42]). A detailed analysis on both devolatilization and char burnout models has been carried out highlighting the best combination of those sub-models in order to achieve a better comparison between the numerical results and the

experimental measurements. In the present work, accurate measurements obtained from a full-scale, swirl-stabilized, aerodynamically-staged, pulverized coal burner have been obtained. All of the experiments have been performed in a stand-alone configuration at the Combustion Environment Research Centre (CCA) of Ansaldo Caldaie S.p.A. in Gioia del Colle (Italy) [43]. The aim of the present work is to provide a reliable prediction model of the coal combustion behavior and pollutant emissions in order to support, by means of numerical tools, the experimental research activity. The model parameters of the coal combustion have been determined according to the coal characteristic without any adjusting procedure linked to the specific experimental test rig. Therefore, the influence of the burner geometry and boundary conditions on the model parameters is expected to be minimized. An assessment of the existing models of devolatilization and char burnout has been made by means of a comparison between the numerical and experimental results.

2. Experimental Activity

The experimental activity refers to a full-scale testing of a pulverized coal burner (Figure 1) for wall-fired steam generators, namely the TEA-C (Three-flux Enel Ansaldo burner), based on the Low-NO_x Burner (LNB) technology, operated in a stand-alone configuration, at the CCA of Ansaldo Caldaie S.p.A., located in Southern Italy (Gioia del Colle, Bari) (Figure 2).

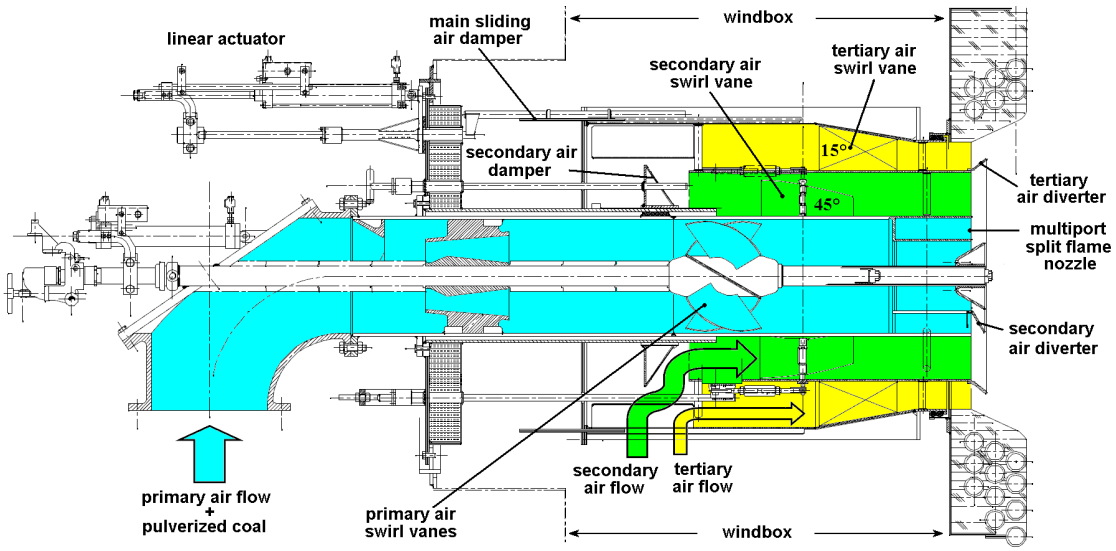

Figure 1. Three air flux coal burner.

Figure 2. Night view of the 48 MW_{th} experimental facility at CCA, Gioia del Colle, Italy.

2.1. The Burner

The LNB technology implemented in the TEA-C burner determines a reduction in NO_x emissions by acting directly on the combustion process. Actually, this is one of the less expensive solutions to reduce NO_x emissions from utility boilers and can also be easily retrofitted in existing steam generators. This LNB reduces emissions by promoting organic nitrogen devolatilization in a sub-stoichiometric environment and generating a stable attached flame at any burner load by means of an effective aerodynamic air-staging. Multiple air registers are implemented in order to delay the mixing of air with coal, which is injected through a coal nozzle in the center of the burner. Primary air carries the pulverized coal from the coal mill to a multi-port split flame nozzle. The secondary air swirled flow inhibits the initial flame to spread radially outward, delaying the mixing of tertiary air with the fuel stream. Tertiary swirled air is then staged for completing the coal combustion. Actually, both secondary and tertiary air flows are swirled counter-clockwise (by means of guide vanes characterized by stagger angles equal to 45° and 15°, respectively), in order to further delay the air fuel mixing generating a longer flame. More details on LNBs can be found on the review work of Bireswar and Amitava [44], which focuses on the different design approaches in the burner technology for reducing NO_x emissions.

2.2. The CCA Test Facility

The CCA main test facility is actually a 48 MW_{th} steam generator, able to be fed with several different fuels (natural gas, eventually with controlled addition of H_2, N_2 and CO_2 in various proportions, light fuel oil (LFO), heavy fuel oil (HFO), Orimulsion®, pulverized coal, biomasses). The combustion chamber is refractory lined, in order to balance the heat extraction and generate the flame thermal boundary conditions and the flame temperature in similarity with the real burner flame. The combustion chamber has a horizontal development and is characterized by a hopper bottom with a dry ash extraction system. Its main dimensions are: height = 5.3 m (excluding the hopper, which is 2.5 m high); width = 4.35 m; length = 12.5 m. Downstream of the combustion chamber, the flue gas flows through a convective pass located at the end of the right-hand side of the boiler, where part of the total steam produced is superheated.

2.3. The Measuring Equipment and Technologies

The test facility is equipped with auxiliaries and instrumentation for a wide range of experimental applications. An airfoil flow meter has been used to measure the secondary and tertiary air flows. This method has been previously validated, comparing the airfoil flow rate measurements against the one contemporaneously performed by means of a Pitot tube, moved along a grid according to the UNI10169 standard: "Emission measurement - Determination of velocity and flow rate in conveyed gas flow by Pitot tube" of the Italian National Association for Standardization (UNI), and obtaining a coefficient of determination, *R*-squared, equal to 0.9989. For primary air flow, an Annubar averaging Pitot tube was used. In this case, during the Annubar characterization, a coefficient of determination, *R*-squared, equal to 0.98640 was obtained. During cold flow tests, the differential pressure transducers placed in the burner wind box and in the mill have been calibrated against U-tube manometers. The control of the pulverized coal mass flow rate is carried out by setting the number of revolutions per minute of the pulverized coal feeding system. The dependency of the mass flow rate versus the number of revolutions per minute was previously characterized storing the pulverized coal on a balance, with density verification. In order to perform the flue gas analysis, four different units are actually used, namely: a Siemens Ultramat 6 (Siemens AG, Munich, Germany), which operates according to the non-dispersive infrared (NDIR) two-beam alternating light principle, for NO (0 –200 mg/m^3) and CO (0–75 mg/m^3); a Siemens Ultramat 23 (Siemens AG, Munich, Germany), which operates according to the NDIR principle, for SO_2 (0–400 mg/m^3); a Siemens Oxymat 6 (Siemens AG, Munich, Germany), which operates according to the paramagnetic alternating pressure principle,

for O_2 (0–21%$_{vol}$); a Siemens Fidamat 6 (Siemens AG, Munich, Germany), which is based on flame ionization detection (FID), for measuring total hydrocarbon concentrations. The exhaust gas is picked up from a grid located upstream of the air heater and directly conveyed (via a heated probe) to the analyzer. The grid is composed of four probes, made according to the standard, each one ending with a silicon carbide filter. Two suction-type pyrometers (CCA, Gioia del Colle, Italy), one equipped with a K-type thermocouple (Tersid, Milano, Italy) and the other with a B-type thermocouple (Tersid, Milano, Italy), are positioned at the exit of the combustion chamber for evaluating the flue gas temperature. For the in-flame measurements, a suction-type pyrometer, equipped with an S-type thermocouple (Tersid, Milano, Italy), was used. The thermocouple has two head shields, the outer one made of titanium alloy, whilst the inner one in alumina. After having positioned the pyrometer at the point of measurement, the products of combustion in the neighborhood of the measuring point are sucked by means of a steam ejector, for a time sufficient to achieve a stable value of the temperature. The steam velocity inside the ejector has been set at that minimum value, which is able to guarantee the independence of the measured temperature, but at the same time, to limit the sampling volume in the neighborhood of the measuring point. After the temperature is acquired, the ejector is turned off, and the gas sampling, for the in-flame species concentration measurements, is performed directly by means of the pump embedded in the gas analyzer. Actually, for the in-flame chemical composition measurements, two portable analyzers are used. The first one is a Siemens Ultramat 23, which measures CO (0– 1250 ppm), NO (0–1000 ppm) and CO_2 according to the NDIR principle, plus O_2 with an electrochemical oxygen measuring cell. The second one is an ABB EL3020 for measuring CO (0–10%) and SO_2 (0–2000 ppm) according to the NDIR principle with the Uras 26 photometer. The data acquisition (over a time period hardly exceeding 5 min, depending on the measuring point and the fuel used, which may cause more or less operating variations) starts only after a stable value of O_2 concentration is registered. The data acquisition system is developed in the LabVIEW programming environment.

3. Numerical Model

The computational domain (Figure 3) includes the primary air duct (Figure 4), the burner nozzle and the combustion chamber. The continuous phase is treated as a continuum by solving the steady, incompressible, three-dimensional RANS equations with a pressure correction approach [45] and a realizable $k - \epsilon$ model [46] for the turbulence closure. Indeed, the flow field is influenced by the buoyancy; therefore, a non-zero gravity field has been considered in the momentum equation. The realizable $k - \epsilon$ model takes into account the generation of turbulent kinetic energy, k, due to the buoyancy, introducing a corresponding contribution in the production of k [47]. Sutherland's viscosity law has been considered in order to deal with the molecular viscosity dependency on temperature. The pressure and viscous terms are discretized by means of a second order centered scheme, whereas convective terms are discretized using the more stable second order upwind scheme. Considering the geometric complexity of the burner (Figure 5), in order to obtain results as accurate as possible and to limit the maximum number of cells, according to a previous work [43], a hybrid multi-block grid was generated with an overall number of cells equal to 4,293,377. Computations have been performed on a workstation with a multicore CPU (Intel® Core™ i7 960 quad core, max frequency 3.20 GHz, 12 GB of RAM, (Intel Corporation, Folsom, CA, USA)); the total CPU-time was equal to 2.4 million of seconds for each simulation.

In order to reduce the computational effort, secondary and tertiary air ducts are simulated separately defining the swirl characteristic of the flow in terms of velocity angle with respect to the axial velocity.

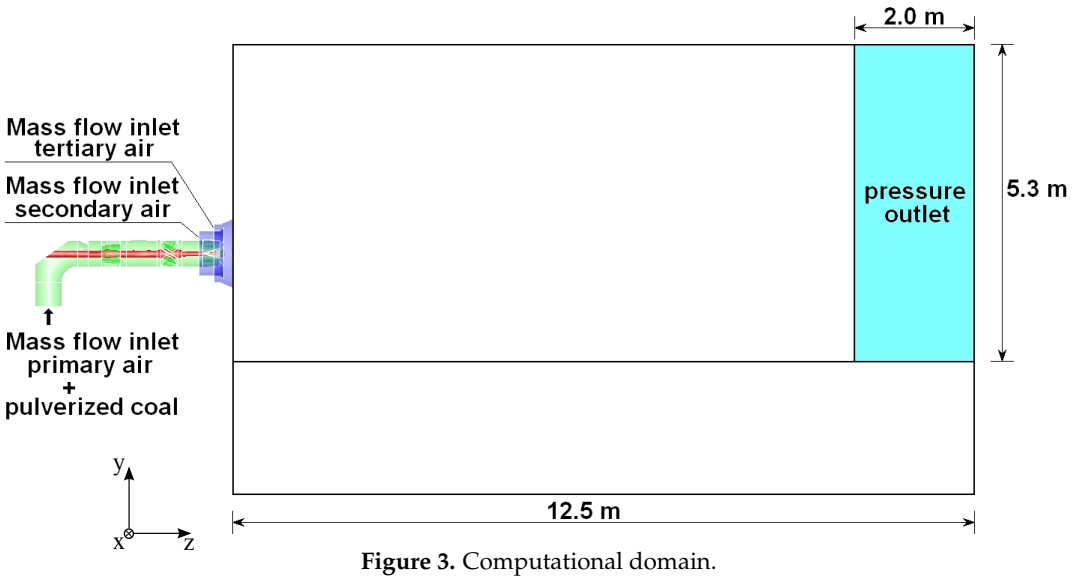

Figure 3. Computational domain.

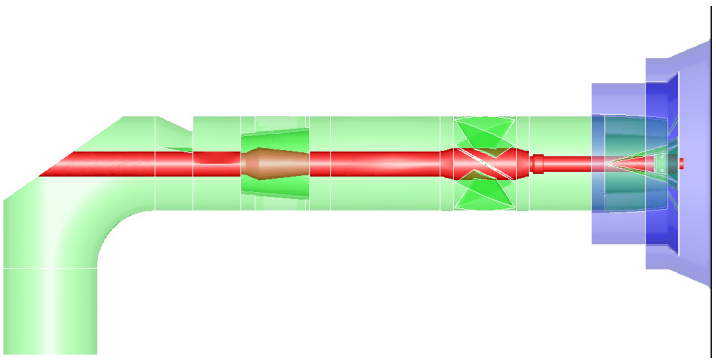

Figure 4. Primary air duct.

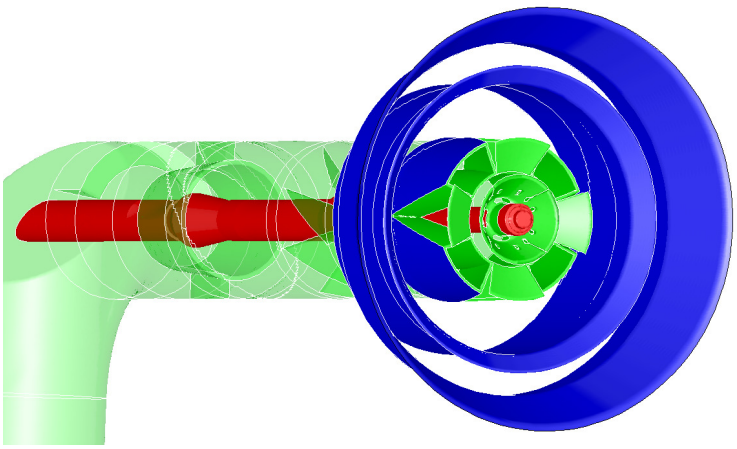

Figure 5. 3D view of the primary air duct.

3.1. Boundary Conditions

The combustion air is split into three different flows, namely primary, secondary and tertiary air. At their inlets, the mass flow rates have been specified, and uniform spatial velocity distributions have been imposed. Concerning the turbulence quantities, they have been specified in terms of turbulence intensity and hydraulic diameter. The primary air stream is characterized by a mass flow rate $G_{a\,1}$ = 9.5 t/h, without any swirl, a temperature $T_{in\,1}$ = 356 K, a turbulence intensity, I_1 = 2%,

and a hydraulic diameter, $D_{h\,1}$ = 0.438 m. The inlet boundary condition related to the secondary air flow is characterized by a mass flow rate $G_{a\,2}$ = 17.5 t/h, with a velocity angle $\alpha_{v\,2}$ = 45° with respect to the axial direction, a temperature $T_{in\,2}$ = 564 K, a turbulence intensity, I_2 = 5%, and a hydraulic diameter, $D_{h\,2}$ = 0.2 m. The tertiary air flow is characterized by a mass flow rate $G_{a\,3}$ = 18.5 t/h, with a velocity angle $\alpha_{v\,3}$ = 15° with respect to the axial direction, a temperature $T_{in\,3}$ = 564 K, a turbulence intensity, I_3 = 5%, and a hydraulic diameter, $D_{h\,3}$ = 0.2 m. The mass flow rate of pulverized coal, G_b, equal to 4.43 t/h is actually carried by the primary air stream. At the domain outlet, a uniform pressure distribution has been imposed. The combustion chamber walls are considered adiabatic. The pulverized coal has been treated as a discrete phase and modeled by means of a two-way coupling Lagrangian approach. The collisions of the coal particles with the combustion chamber walls have been treated as inelastic. The particle distribution at the domain inlet and the coal characteristics are based on the pulverized coal actually used in the experimental test. The used pulverized coal is a bituminous, inertinite-rich, pulverized coal coming from Kleinkopje's mine in South Africa. It was milled and than classified by means of a rotating sieve at 200 rpm (99.90% with $d < 300$ µm, 99.45% with $d < 150$ µm, 90.00% with $d < 75$ µm). Therefore, a Rosin–Rammler distribution of spherical particles is considered with the distribution parameters reported in Table 1, which accurately represent the measured data (Figure 6).

Table 1. Rosin–Rammler distribution parameters.

Parameter	Symbol	Value	Unit
Mean diameter	D_{mean}	40	µm
Max diameter	D_{max}	300	µm
Min diameter	D_{min}	5	µm
Spread parameter	n	1.31	-
Number of classes	N	10	-

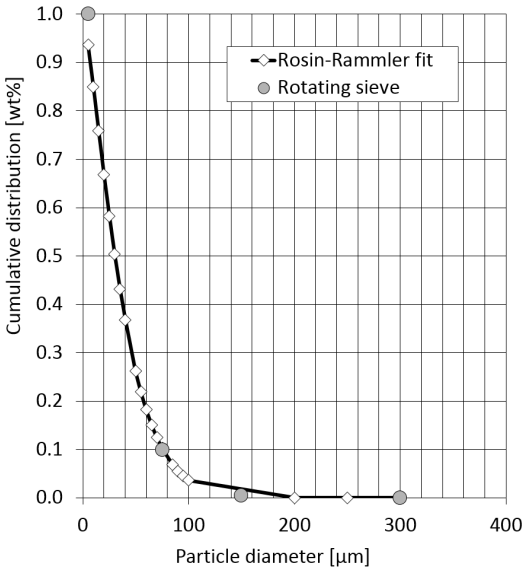

Figure 6. Kleinkopje's coal particle distribution.

3.2. Radiation Heat Transfer

Radiation heat transfer has been accounted for by means of the P-1 model, based on the first order spherical harmonic expansion of the radiation intensity [48,49], together with the cell-based Weighted-Sum-of-Gray-Gases Model (WSGGM) for the radiative properties of the gases. Particle emissivity and particle scattering are both taken equal to 0.9.

3.3. Pulverized Coal Combustion

The pulverized coal combustion process has been subdivided into the following steps: (i) inert heating; (ii) devolatilization and swelling; (iii) volatile matter combustion (homogeneous combustion in the continuous phase); (iv) char burnout (heterogeneous combustion). The inert heating laws are applied when the particle temperature is less than the assigned vaporization temperature, T_{vap}, and when the volatile fraction, f_{v0}, of the discrete phase vanishes. The devolatilization law is applied when the temperature of the particle reaches the vaporization temperature, T_{vap} = 600 K, untill the mass of the particle, m_p, exceeds the mass of the non-volatiles in the particle. Furthermore, during the devolatilization process, the particle swelling has been taken into account by means of a swelling coefficient, C_{sw}, equal to 1.5, considering that for Kleinkopje's coal, this value can range between zero and three [50].

3.3.1. Devolatilization Models

Due to the sensitivity of the burner performance on devolatilization, in the present work, two devolatilization models have been considered: the single kinetic rate (SKR) model and the chemical percolation devolatilization (CPD) model. Volatile turbulent combustion has been simulated using the non-premixed modeling approach [51].

Single Kinetic Rate Model

The SKR model [52] assumes that the rate of devolatilization is linearly dependent on the amount of volatiles remaining in the particle. Despite its simplicity, this model does not take into account the heating rate of the coal particle. Furthermore, the kinetic parameters (i.e., the activation energy, E_a, and the pre-exponential factor, A) are empirically determined. In the present work, the values of the Arrhenius parameters for the SKR model are: $E_a = 7.40 \times 10^7$ J/kmol; $A = 2 \times 10^5$ s^{-1}. These values have been averaged from the corresponding values of two different weakly-swelling coals, namely B and C from Badzioch and Hawksley [52].

Chemical Percolation Devolatilization Model

In order to characterize the devolatilization process under rapid heating conditions, unlike the single kinetic rate model, the CPD model considers the thermo-chemical transformations of the coal structure rather than using empirical relationships [53–55]. Most of the variables introduced in the CPD model are coal independent [55], and only five are coal-specific parameters, which can be obtained by means of solid-state ^{13}C Nuclear Magnetic Resonance (NMR) spectroscopy [56]. The CPD parameters of Kleinkopje's coal have been taken equal to the ones of Highveld's coal, similarly to what has been done by Grant et al. [57]. This choice is based on the similarities between the two coals [58,59], being both inertinite-rich (see Table 2 for maceral composition) and presenting very similar ultimate analyses. Table 3 compares the ultimate analyses of both Kleinkopje's coal, burned during the experimental tests at CCA, and Highveld's coal [56]. For completeness, their proximate analyses are reported in Table 4. Actually, except the side chain molecular weight, MW_δ, all of the CPD model parameters used in the present work (summarized in Table 5) are taken from the work of van Niekerk et al. [56]. Concerning the side chain molecular weight, MW_δ (not available in the work of van Niekerk et al. [56]), being dependent on the coal rank, its value has been averaged from a value set [55] of other bituminous coals.

Table 2. Maceral composition (volume % mmf basis).

Coal Origin	Vitrinite %	Inertinite %	Liptinite %
Kleinkopje [59]	35.4	62.3	2.3
Highveld [60]	11.2	87.7	1.1

Table 3. Ultimate analysis (weight % dmmf basis).

Coal Origin	C	H	O	N	S
Kleinkopje (Lab analysis)	83.77	4.49	9.31	1.89	0.53
Highveld [60]	83.72	4.53	8.9	1.97	1.99

Table 4. Proximate analysis (weight % dry basis).

Coal Origin	Ash	Volatile	Fixed Carbon
Kleinkopje (Lab analysis)	13.97	24.46	61.57
Highveld [60]	28.11	24.44	47.45

Table 5. Coal-specific parameters for the CPD model.

Parameter	Symbol	Value	Unit
Initial fraction of bridges in the coal lattice [56]	p_0	0.83	-
Initial fraction of char bridges [56]	C_0	0	-
Lattice coordination number [56]	$\sigma + 1$	5.2	-
Cluster molecular weight [56]	MW_1	308	kg/kmol
Side chain molecular weight [55]	MW_δ	30	kg/kmol

3.3.2. Char Burnout Models

Char burnout models consider coal as composed of porous spherical grains. Every grain may be described by a carbon matrix with the remaining chemical elements and the inert mineral phase defined in the ultimate analysis, uniformly distributed. Char burnout is supposed to occur strictly after devolatilization is completed. During the heterogeneous surface reaction, the solid combustible fraction of the particle is oxidized into CO. In this work, both the kinetic/diffusion-limited surface reaction rate model and the intrinsic model have been considered.

Kinetic/Diffusion-Limited Surface Reaction Rate Model

The kinetic/diffusion-limited surface reaction rate model is a pseudo-kinetic model based on the theories of Baum and Street [61] and Field [62], in which a diffusion rate coefficient, D_0, and a kinetic rate coefficient, R, are weighted to yield a char combustion rate. The particle size is assumed to remain constant in this model, while the density is allowed to decrease. The values used in the present work are reported in Table 6.

Table 6. Kinetic/diffusion-limited surface reaction rate model parameters.

Parameter	Symbol	Value	Unit
Mass Diffusion-Limited Rate Constant	C_1	5×10^{-12}	-
Kinetic-Limited Rate Pre-Exponential Factor	C_2	6.7	-
Kinetic-Limited Rate Activation Energy	E_a	1.1382×10^8	J/kmol

Intrinsic Model

The intrinsic model [47] computes the heterogeneous reaction rate considering both kinetics and diffusion phenomena. Actually, the kinetic rate is explicitly expressed in terms of the intrinsic chemical and pore diffusion rates. To allow a more adequate description of the char particle size and density variations during combustion, the burning mode has been specified relating the char particle diameter to the fractional degree of burnout [47]. The default kinetic rate parameters have been considered. Char porosity has been computed considering both true and apparent densities [63,64]. Knowing that Kleinkopje's coal is dominated by macropores ($r_p > 150$ Å) [65], the default r_p value has been

considered plausible. Finally, an estimated mean value for the specific internal surface area, A_g, in bituminous coal was considered [66]. The main model parameters are summarized in Tables 7 and 8.

Table 7. Parameters for the char burnout intrinsic model.

Parameter	Symbol	Value	Unit
Mass Diffusion-Limited Rate Constant	C_1	5×10^{-12}	-
Kinetic-Limited Rate Pre-Exp. Factor	A_i	0.0302	-
Kinetic-Limited Rate Activ. Energy	E_i	1.794×10^8	J/kmol
Char porosity	θ	0.67	-
Mean pore radius	r_p	6×10^{-8}	m
Specific internal surface area	A_g	300,000	m^2/kg
Tortuosity	τ	1.4142	-
Burning mode	α	0.2500	-

Table 8. Other parameters for the char burnout intrinsic model.

Parameter	Symbol	Value	Unit
Coal density	ρ	1300	kg/m^3
Coal specific heat	c_p	1380	J/(kgK)
Low heating value	LHV	3.29×10^7	J/kg

3.4. NO_x Emission Models

In order to predict NO_x emissions, a transport equation for nitric oxide (NO) concentration has been solved. The NO_x formation has been evaluated according to the thermal and fuel-NO mechanisms; hence, two additional transport equations for intermediate species (HCN and NH_3) have been considered. The NO_x transport equations are solved in post-processing based on a frozen flow field and combustion solution. The LNB under investigation, by implementing an aerodynamic internal air staging rather than a fuel staging, does not show any significant NO_x re-burning. In fact, for this burner, the flow residence time is not long enough (actually, significantly lower than 0.4 s) in the fuel-rich stoichiometry region, where NO_x re-burning can occur. For this reason, no re-burning has been taken into account in the NO_x modeling.

3.4.1. Thermal NO_x Model

The formation of thermal NO_x is determined according to the extended Zeldovich mechanism, and the rate constants have been selected based on the evaluation of Hanson and Salimian [67]. The needed concentrations of O, H and OH have been taken directly from the local species mass fractions.

3.4.2. Fuel NO_x Model

Organic compounds present in coal and containing nitrogen can significantly contribute to the total NO_x formed during the combustion process. Fuel nitrogen is split between volatiles and char during coal devolatilization and in the nitrogen conversion can originate hydrogen cyanide (HCN) and/or ammonia (NH_3). Local NH_3 and HCN concentrations derive from the solution of the respective transport equations solved in post-processing according to the kinetics developed by De Soete [68]. With bituminous coal, better NO_x predictions are obtained when using an HCN/NH_3 partition ratio of 9:1. The nitrogen contained in the char is then heterogeneously oxidized to NO via an overall reaction.

4. Results

In this paper, fully-three-dimensional coal combustion simulations have been performed varying both the devolatilization and the char burnout models. In the literature, several models exist; therefore, the objective of this work is to assess against the experiments the best combination of

them. Two different devolatilization models, the CPD model and the Single Kinetic Rate (SKR) model, and two different char burnout models, the Intrinsic (Int) model and the Kinetic/Diffusion surface reaction rate (KD) model, have been considered. An overview of the models adopted with respect the simulation case is reported in Table 9.

Table 9. Details of the models included in the present test cases. Int: Intrinsic; KD: Kinetic/Diffusion; SKR: Single Kinetic Rate.

Simulation	Devolatilization	Char Burnout
1	CPD	Int
2	CPD	KD
3	SKR	Int
4	SKR	KD

Results are given in terms of devolatilization and char burnout rates, temperature, CO and NO emissions, contoured on a vertical meridian plane (Plane DD) and on three different orthogonal planes (Plane AA, Plane BB, Plane CC) distant respectively 800 mm, 1181 mm, 2095 mm, from the combustion chamber wall close to the burner nozzle. In order to compare the numerical results with the experimental data, contour plots of temperature and species molar concentrations (in particular O_2, CO_2, CO and NO) are considered along three different horizontal traverses intercepting the burner axis, A, B and C, placed 800 mm, 1181 mm and 2095 mm away from the combustion chamber wall close to the burner nozzle, respectively. Finally, the NO rates of formation have been evaluated, along the same three traverses.

4.1. Simulation 1: CPD-Int Models

Here, the CPD model and the Intrinsic char burnout (Int) model are considered. From devolatilization contours (Figure 7a), an asymmetry in the flame structure can be highlighted. This is due to the pulverized coal distribution, which is not perfectly uniform at the burner nozzle, but slightly less concentrated on the right (facing the burner). This result confirms that the particle distribution has an important role in the description of the flame behavior. Thus, the simulation of the primary flow, where the particles are seeded and then convected, is crucial for the correct analysis of the burner performance. In fact, the pulverized coal is deflected in the primary air duct elbow (Figure 1), leading to an increased concentration of particles in the upper part of the primary duct rather than in the lower one. The following diffuser and swirling foils are not able to redistribute uniformly the coal particles in the azimuthal direction. The pulverized coal is just swirled counter-clockwise (facing the burner), and the zone with a reduced concentration is rotated on the right. These consideration on the particle distribution at the burner inlet are valid for all of the simulations performed in this study, being not influenced by the combustion models implemented. At Traverse C, the devolatilization process is almost complete. The contours of char burnout (Figure 7b) show that this process goes further downstream and is particularly intense where the pulverized coal meets secondary and tertiary air flows. Buoyancy brings up light char and warmer gases, where further burnout can occur. Looking at the Transversal Sections AA, BB and CC of Figure 7b, there is a local burnout peak shifted clockwise (facing the burner) with respect to the meridian plane (DD). This behavior is related to the clockwise rotation of the flow in the outermost part of the combustion chamber. Moreover, due to the buoyancy effect, the char burnout rate peak is in the upper part of the combustion chamber. It is worth noting that the highest char burnout rates occur in the first 4 m of the combustion chamber. The temperature field (Figure 7c) shows that the highest temperature occurs in the region where the secondary and tertiary air flows and the char are mixed together. The presence of an outermost clockwise motion (facing the burner) of the flue gases causes an asymmetric temperature field in the orthogonal planes (AA, BB, CC). The flame core has the highest values of CO concentration where partially-burned volatile matter recirculates toward the burner nozzle (Figure 7d), and the oxygen of secondary and

tertiary air flows is not yet involved in the combustion process. The maximum NO concentration reaches a value of 1000 ppm. It occurs where both char burnout and temperatures are the highest (Figure 7e). Downstream, dilution with secondary and tertiary air reduces the NO concentration.

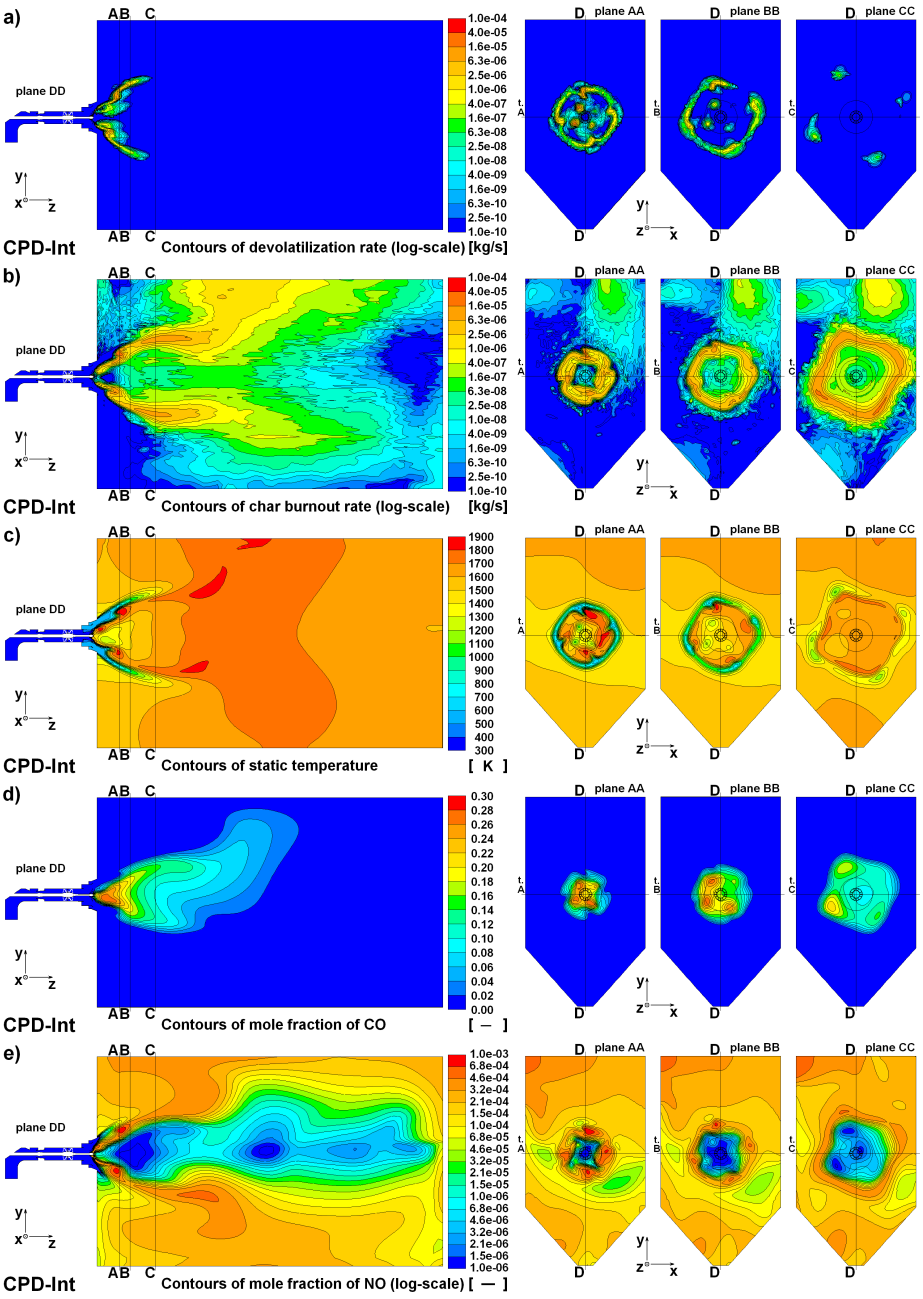

Figure 7. Results obtained by means of the CPD-Int model. (**a**) Devolatilization rate; (**b**) char burnout rate; (**c**) static temperature; (**d**) mole fraction of CO; and (**e**) mole fraction of NO.

4.2. Simulation 2: CPD-KD Models

In this second test, the char burnout model is changed from the Intrinsic (Int) to the more empirical Kinetic/Diffusion-limited surface reaction rate (KD) model retaining the CPD devolatilization model used in the previous case. The results show that there is almost no variation on the extension of the region involved in the devolatilization process (Figure 8a), even though peaks are less intense and an increase of devolatilization in the first part of the flame core can be noticed. The char burnout rate highlights the main differences with respect to Simulation 1 (Figure 8b); burnout reaches lower

rates, but is more diffused within the combustion chamber, extending to the high temperature zone at least 1 m downstream (Figure 8c). Due to a partial devolatilization in the first part of the flame core, in this reducing zone, there is a significant formation of carbon monoxide (Figure 8d). Since the highest temperatures are predicted in low oxygen regions, globally, the NO mole fractions are lower than the ones predicted when the intrinsic model is used (Figure 8e).

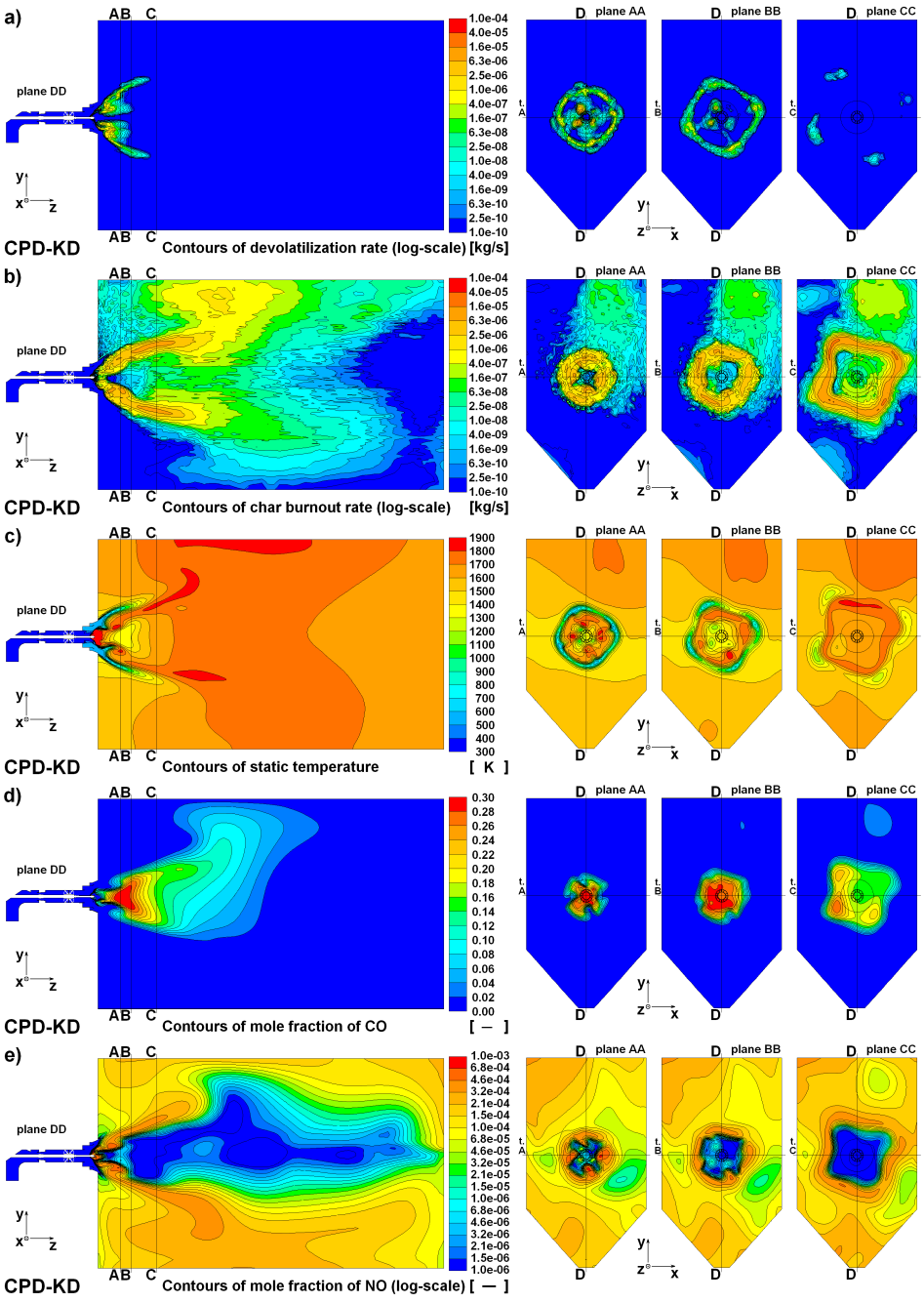

Figure 8. Results obtained by means of the CPD-KD model. (**a**) Devolatilization rate; (**b**) char burnout rate; (**c**) static temperature; (**d**) mole fraction of CO; and (**e**) mole fraction of NO.

4.3. Simulation 3: SKR-Int Models

Here, the empirical Single Kinetic Rate (SKR) model and the Intrinsic model (Int) are used as the devolatilization and char burnout model, respectively. The SKR model assumes that the rate of devolatilization is linearly dependent on the amount of volatiles remaining in the particle. Even though

the spatial distribution of the devolatilization field has not changed, nonetheless, with the SKR model, the devolatilization rates are higher with respect to those predicted in Simulations 1 and 2 (Figure 9a). Therefore, the char burnout process (Figure 9b) is accelerated. Higher temperatures are reached (Figure 9c), but at the same time, inside the combustion chamber, the temperature gradients are smoothed. This faster devolatilization process reduces the quantity of volatiles in the flame core; hence, a lower CO concentration is predicted to occur in this zone (Figure 9d). Furthermore, since there is a higher quantity of volatile matter in regions at high temperature and a higher oxygen content (coming from secondary and tertiary air flow streams), the NO formation is promoted (Figure 9e) in these zones.

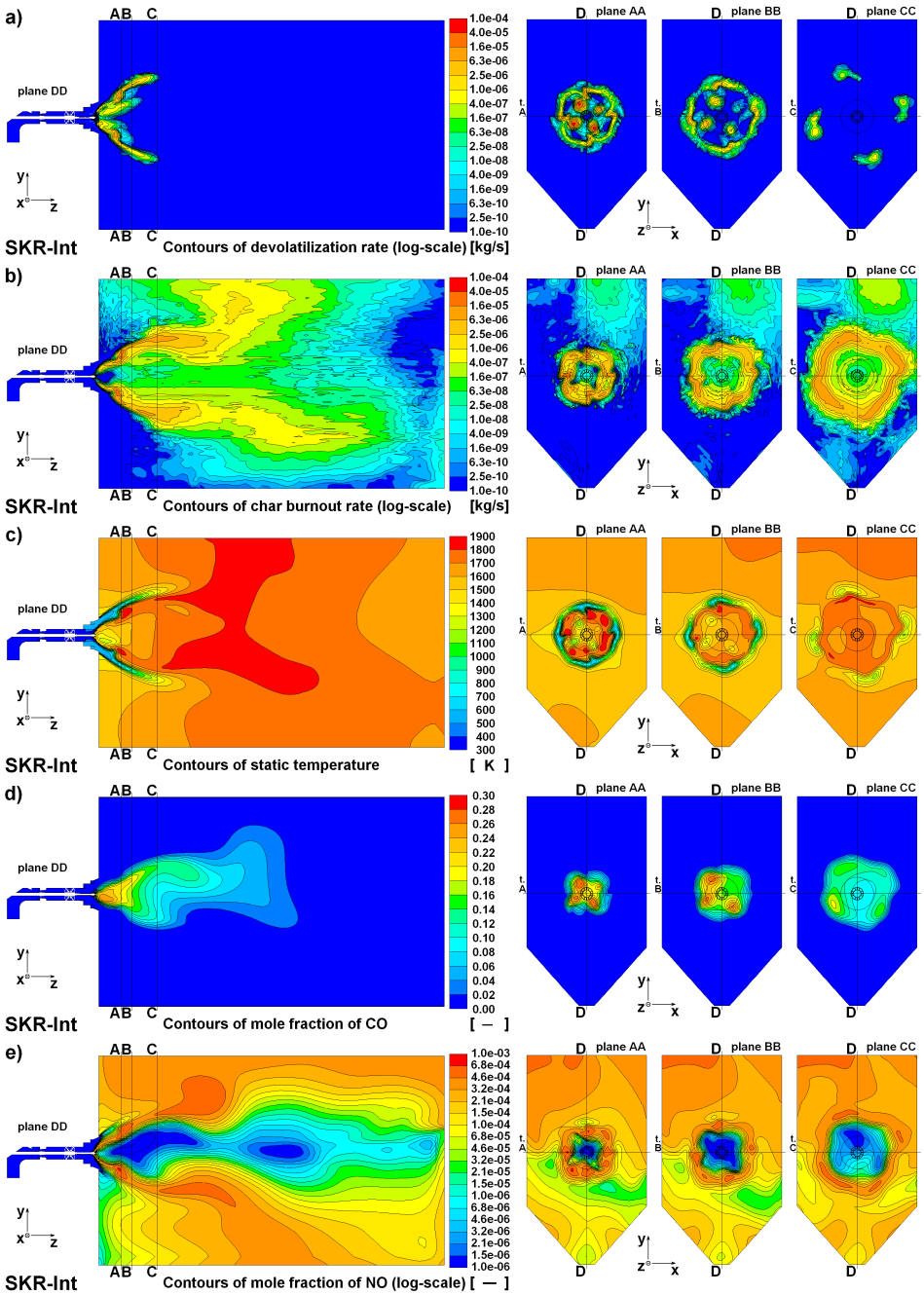

Figure 9. Results obtained by means of the SKR-Int model. (**a**) Devolatilization rate; (**b**) char burnout rate; (**c**) static temperature; (**d**) mole fraction of CO; and (**e**) mole fraction of NO.

4.4. Simulation 4: SKR-KD Models

In this simulation, the Single Kinetic Rate (SKR) devolatilization model and the Kinetic/Diffusion-limited surface reaction rate (KD) char burnout model have been considered. The characteristics of SKR and KD model depicted in Simulations 2 and 3 act together. Both devolatilization (Figure 10a) and char burnout (Figure 10b) are intensified, and higher temperatures are reached inside the combustion chamber (Figure 10c). Due to the KD char burnout model, here again, there is a heterogeneous combustion in the first part of the flame core, giving origin to a high concentration of carbon monoxide in the flame core (Figure 10d). Finally, there is an increment of NO formation (Figure 10e) due to the faster devolatilization computed by the SKR model, even though it is less than the SKR-Int case, due to the effect of the KD model.

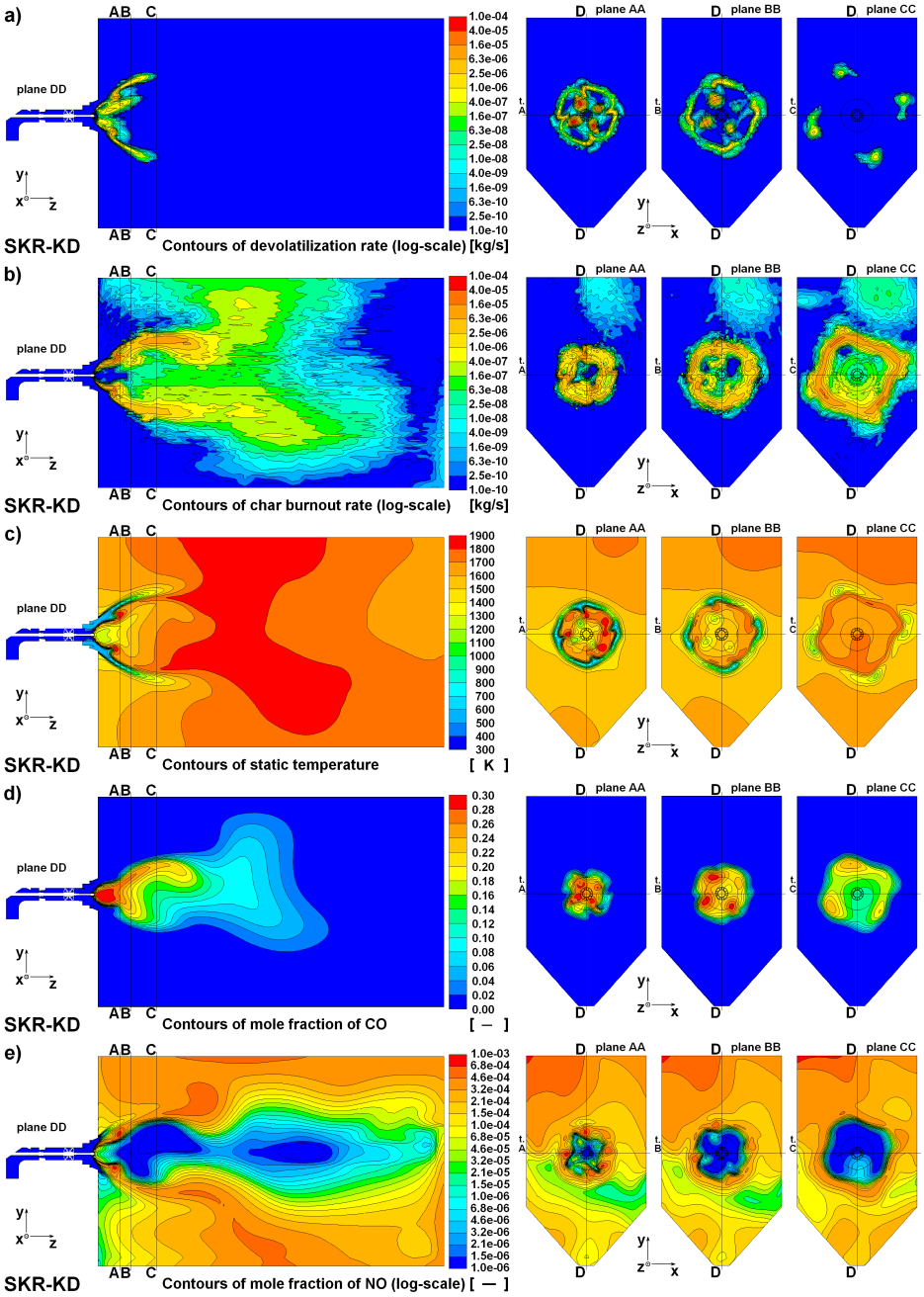

Figure 10. Results obtained by means of the SKR-KD model. (**a**) Devolatilization rate; (**b**) char burnout rate; (**c**) static temperature; (**d**) mole fraction of CO; and (**e**) mole fraction of NO.

4.5. Rate of Formation of NO_x

Considering the rate of formation of NO along three different traverses, it is possible to ascertain that the main contribution to the NO emission is due to the fuel-NO_x mechanism (Figure 11). Moving downstream (at Traverses B and C), all of the simulations show similar performance in terms of NO rate prediction. In the near field, close to the burner nozzle (at Traverse A), there are the most significant differences. The NO re-burning, where negative rates of NO appear, is enhanced considering the kinetic/diffusion-limited surface reaction rate char burnout model, which implies the evaluation of a lower value of NO emissions at the exit (Table 10).

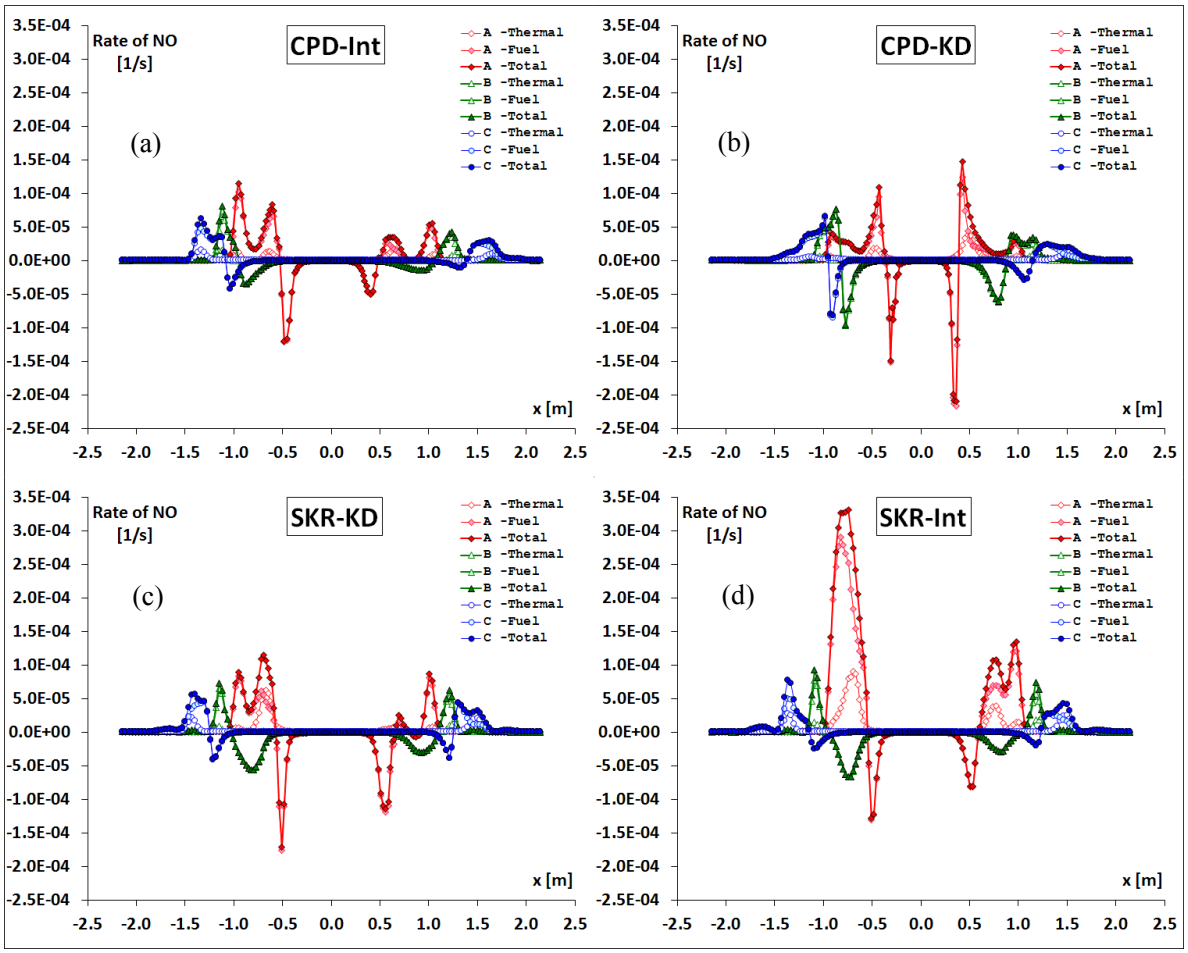

Figure 11. NO rate distribution evaluated at Traverses A, B and C according to the different CFD models. (**a**) CPD-Int; (**b**) CPD-KD; (**c**) SKR-KD; and (**d**) SKR-Int.

Table 10. Area weighted averaged value at the exit.

Parameter	Unit	CPD-Int	CPD-KD	SKR-Int	SKR-KD
Temperature	K	1641	1674	1698	1715
O_2 mole fraction	-	0.02973	0.02341	0.02828	0.02361
CO_2 mole fraction	-	0.1548	0.1600	0.1560	0.1599
H_2O mole fraction	-	0.04944	0.05116	0.04981	0.05108
NO concentration	ppm	180.9	150.2	234.7	267.2

4.6. Assessment of the Models

In order to evaluate which combination of devolatilization and char burnout models is more appropriate for the simulation of the pulverized coal burner under investigation, the numerical results

have been compared with the experimental data acquired on three different traverses (A, B and C) close to the burner nozzle. The traverses, where the probes are located, are horizontal and normal to the nozzle axis (Figure 12).

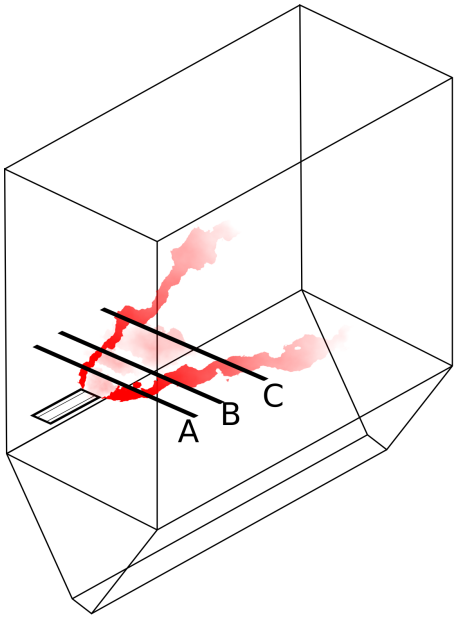

Figure 12. Schematic of the position of Traverses A, B and C within the burner geometry along with the probes placed.

4.6.1. Temperature and O_2

When considering both temperature and oxygen distributions along the three traverses, all of the models give numerical results that are in fairly good agreement with experimental data (Figures 13 and 14).

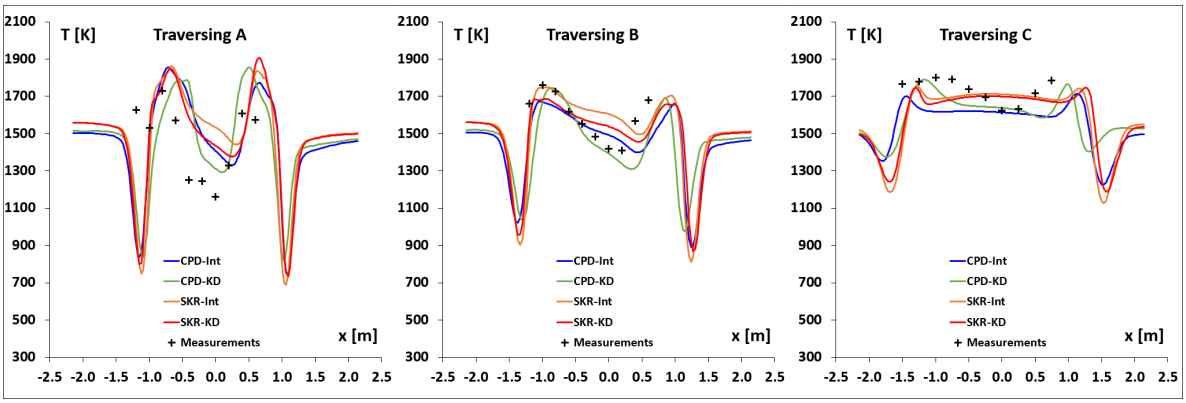

(**a**) (**b**) (**c**)

Figure 13. Temperature distribution along Traverses A (**a**), B (**b**) and C (**c**).

The main differences between the different cases have been found in the near field (at Traverse A). In particular, the CPD-Int model gives a better estimation of the flame core width according to the experimental data, as can be seen in Figure 14. Thus, the increase of the oxygen concentration on the left side, with respect to the burner axis, is well reproduced for both Traverses B and C.

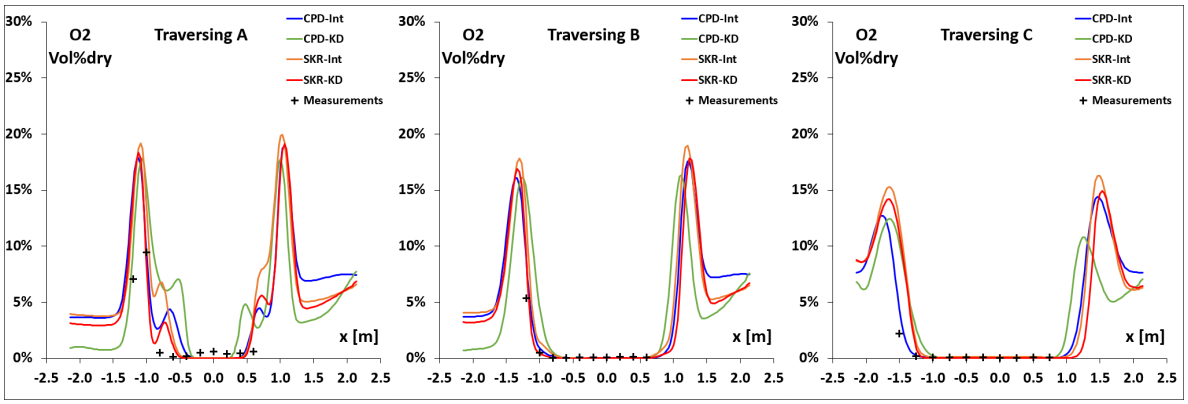

(**a**) (**b**) (**c**)

Figure 14. O_2 molar concentrations distribution along Traverses A (**a**), B (**b**) and C (**c**).

4.6.2. CO and CO_2

In Figure 15, the CO_2 molar concentration highlights the near field differences between the numerical and experimental data. The results show an underestimation of the CO_2 concentration for $0 < x < 0.5$ m of the numerical models with respect to the measurements.

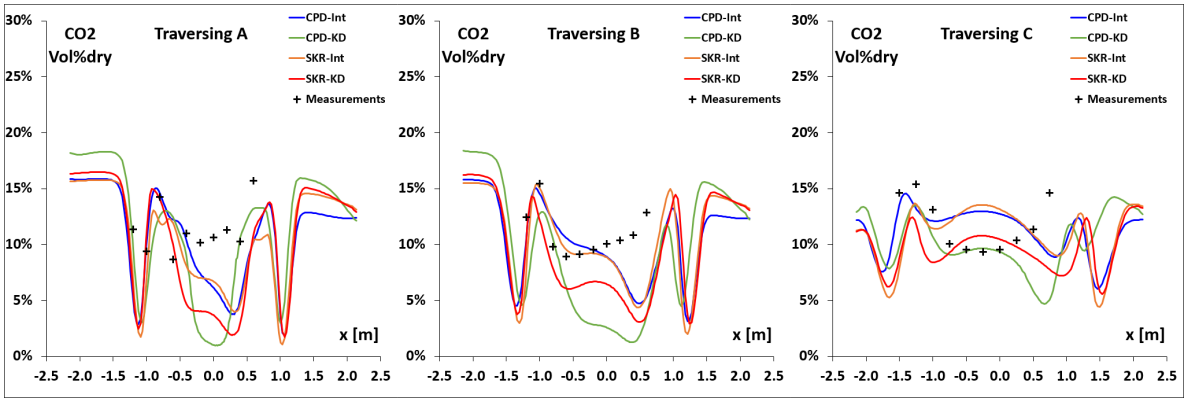

(**a**) (**b**) (**c**)

Figure 15. CO_2 molar concentrations distribution along Traverses A (**a**), B (**b**) and C (**c**).

The CPD-Int and SKR-Int models have a better behavior in the core region near the burner nozzle (Traverses A and B). In the far field (Traverse C), less differences between the different models can be evidenced. On the other hand, the CO distribution, reported in Figure 16, shows an overestimation of the concentration with respect to the experimental data, notwithstanding the applied devolatilization model.

As reported in Figure 16, only a few points correctly acquire the CO concentration. According to the high CO concentration in the flame core, the sensor used in the experiments has been saturated. The CO_2 and CO concentrations reproduced by the models show an underestimation and an overestimation, respectively, compared to the measurements. However, the spatial distribution of the sum of CO_2 and CO concentrations compensate each other, as reported in Figure 17. The near field (Traverses A and B) shows the higher differences between numerical and experimental data with respect to the far field (Traverse C). Even in this case, the effect of CO measurement saturation in the core region affects the experimental measurements. Better results have been obtained when the intrinsic char burnout model has been considered.

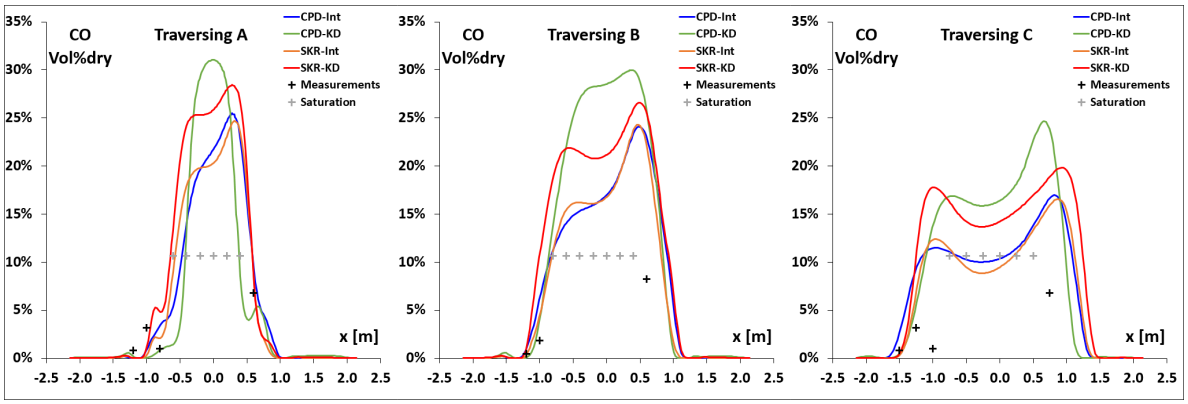

(**a**) (**b**) (**c**)

Figure 16. CO molar concentrations distribution along Traverses A (**a**), B (**b**) and C (**c**).

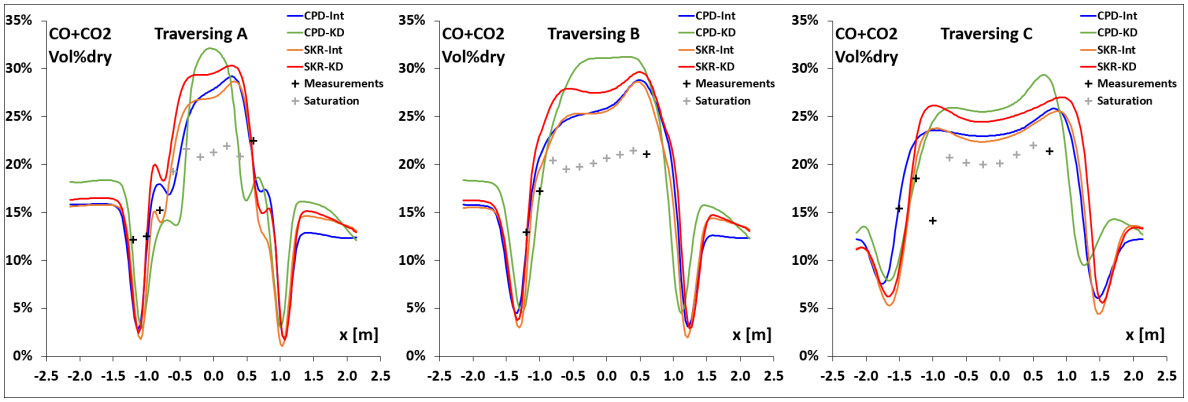

(**a**) (**b**) (**c**)

Figure 17. CO + CO_2 molar concentrations distribution along Traverses A (**a**), B (**b**) and C (**c**).

4.6.3. NO

Then, the quantification of NO emissions is satisfactory, particularly along the two furthest traverses (B and C) from the burner nozzle. As a matter of fact, along these two traverses, there is a quite good agreement not only qualitatively, but also quantitatively (Figure 18). In the near field (Traverse A), the numerical models show two symmetrical peaks of NO concentration with respect to the nozzle axis, which overestimate the measured experimental data, whereas near the nozzle axis (-0.5 m $< x <$ 0.5 m), the numerical models underestimate the NO concentration. However, since Traverse A is very close to the nozzle, a higher difference between the numerical simulation and the experiment is expected due to the higher velocity gradient at the inlet. Indeed, in the injection region, the shear layer induces flow instabilities and a high turbulent flow. The turbulence affects heavily the diffusivity of the species as reported in the experiments compared to the numerical results. Therefore, a more detailed discretization of the near field seems to be needed, but due to numerical resource constraints, the present simulations represent a compromise. Even for NO, the CPD-Int model has the best agreement with the experiments.

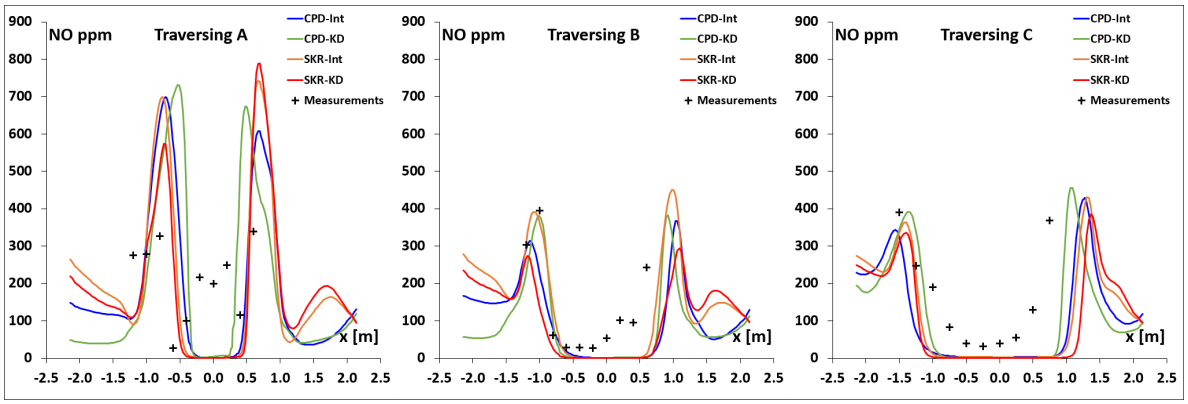

(**a**) (**b**) (**c**)

Figure 18. NO molar concentrations distribution along Traverses A (**a**), B (**b**) and C (**c**).

5. Conclusions

In this study, numerical simulations of a pulverized coal burner have been performed in order to assess the influence of the devolatilization and char burnout models on the performance of a pulverized low-NO_x coal burner. The numerical domain reproduces the geometry of a full-scale, swirl stabilized, aerodynamically staged, burner tested under stand alone configuration at the CCA of Ansaldo Caldaie S.p.A. in Gioia del Colle (Italy). The whole primary air duct has been simulated in order to describe the particles' distribution at the inlet avoiding any assumptions. A Lagrangian-Eulerian approach has been used to trace the particle trajectories within the continuous flow, whereas the combustion process has been split using a multi-step approach that includes: inert heating of the coal particles; devolatilization of the coal; volatile matter combustion in the continuous phase; char burnout. The devolatilization and the char burnout phases have been implemented in the numerical procedure according to different models. Thus, either the SKR or the CPD model has been considered for devolatilization, whereas either the kinetic/diffusion-limited surface reaction rate or the intrinsic char burnout model has been applied for the char burnout. The flow field has been analyzed in terms of devolatilization and char burnout rates, temperature, CO and NO emissions. All of the combinations of devolatilization and char burnout models produce reliable results in terms of temperature and O_2 concentration, whereas the CO, CO_2 and NO concentrations show sensible differences. The combination of the CPD and the intrinsic char burnout models has a better agreement with the experimental results, especially near the nozzle, whereas far from the nozzle, the differences between those models are smaller. The numerical simulation has been able to predict both qualitatively and quantitatively the NO_x formation measured in the experimental test. The results highlight that, in the region closest to the inlet, all of the models show a defect of diffusivity that should be ascribed to the higher turbulence level reached in the experiments. However, the numerical and experimental results are in good agreement, looking at the measurements located immediately downstream. There, the turbulence diffusivity of the numerical model is able to diffuse the species according to the physical behavior measured in the experimental facility. Finally, we can infer that the numerical approach used in this work is able to predict the correct behavior of a pulverized coal burner as confirmed by the comparison with the experimental data. Moreover, the CPD together with the intrinsic char burnout model is able to describe in a better way the temperature field and the species' concentrations in the region close to the nozzle with a better description of the flame core. Since the model parameters have been evaluated a priori, the numerical approach proposed here is expected to be more general and valid for other pulverized coal burner geometries; however, further investigations are planned to confirm this remark.

Acknowledgments: We would like to express thanks to Thomas Giani, from Ansaldo Caldaie, who helped us in the definition of secondary and tertiary air flow stream characteristics.

Author Contributions: Marco Torresi conceived of and directed the research. Marco Torresi and Francesco Fornarelli set up the numerical models, performed the numerical simulations, analyzed the results and wrote the paper. Bernardo Fortunato and Sergio Mario Camporeale discussed the results and contributed with their comments to the writing of the paper. Alessandro Saponaro set up and performed the experiments.

Conflicts of Interest: The authors declare no conflict of interest.

Abbreviations

G_{a1}	Primary mass flow rate
T_{in1}	Primary inlet temperature
I_1	Primary turbulence intensity
D_{h1}	Primary hydraulic diameter
G_{a2}	Secondary mass flow rate
α_{v2}	Secondary velocity angle
T_{in2}	Secondary inlet temperature
I_2	Secondary turbulence intensity
D_{h2}	Secondary hydraulic diameter
G_{a3}	Tertiary mass flow rate
α_{v3}	Tertiary velocity angle
T_{in3}	Tertiary inlet temperature
I_3	Tertiary turbulence intensity
D_{h3}	Tertiary hydraulic diameter
G_b	Coal mass flow rate
T_{vap}	Vaporization temperature
f_{v0}	Volatile fraction
m_p	Particle mass
C_{sw}	Swelling coefficient
E_a	Arrhenius activation energy
A	Arrhenius pre-exponential factor
D_0	Diffusion rate coefficient
R	Kinetic rate coefficient
C_1	Mass diffusion-limited rate constant
A_i	Kinetic-limited rate pre-Exp. factor
E_i	Kinetic-limited rate Activ. energy
θ	Char porosity
r_p	Mean pore radius
A_g	Specific internal surface area
τ	Tortuosity
α	Burning mode
ρ	Coal density
c_p	Coal specific heat
mmf	mineral matter free
$dmmf$	dry mineral matter free
LHV	Low heating value

References

1. BP Statistical Review of World Energy, June 2016. Available online: https://www.bp.com/content/dam/bp/pdf/energy-economics/statistical-review-2016/bp-statistical-review-of-world-energy-2016-full-report.pdf (acessed on 2 January 2017).
2. World Energy Outlook 2015, 10 November 2015. Available online: https://www.iea.org/bookshop/700-World_Energy_Outlook_2015 (acessed on 2 January 2017).
3. BP Energy Outlook 2016 Edition, Outlook to 2035. Available online: https://www.bp.com/content/dam/bp/pdf/energy-economics/energy-outlook-2016/bp-energy-outlook-2016.pdf (acessed on 2 January 2017).
4. Torresi, M.; Saponaro, A.; Camporeale, S.M.; Fortunato, B. CFD analysis of the flow through tube banks of HRSG. In Proceedings of the ASME Turbo Expo, Berlin, Germany, 9–13 June 2008; pp. 327–337.
5. Fornarelli, F.; Oresta, P.; Lippolis, A. Flow patterns and heat transfer around six in-line circular cylinders at low Reynolds number. *JP J. Heat Mass Transf.* **2015**, *11*, 1–28.
6. Fornarelli, F.; Oresta, P.; Lippolis, A. Buoyancy Effect on the Flow Pattern and the Thermal Performance of an Array of Circular Cylinders. *J. Heat Transf.* **2016**, *139*, 022501.

7. Fornarelli, F.; Camporeale, S.M.; Fortunato, B.; Torresi, M.; Oresta, P.; Magliocchetti, L.; Miliozzi, A.; Santo, G. CFD analysis of melting process in a shell-and-tube latent heat storage for concentrated solar power plants. *Appl. Energy* **2016**, *164*, 711–722.
8. Vascellari, M.; Cau, G. Influence of turbulence-chemical interaction on CFD pulverized coal MILD combustion modeling. *Fuel* **2012**, *101*, 90–101.
9. Schaffel, N.; Mancini, M.; Szlęk, A.; Weber, R. Mathematical modeling of MILD combustion of pulverized coal. *Combust. Flame* **2009**, *156*, 1771–1784.
10. Jovanovic, R.; Milewska, A.; Swiatkowski, B.; Goanta, A.; Spliethoff, H. Sensitivity analysis of different devolatilisation models on predicting ignition point position during pulverized coal combustion in O_2/N_2 and O_2/CO_2 atmospheres. *Fuel* **2012**, *101*, 23–37.
11. Jovanovic, R.; Milewska, A.; Swiatkowski, B.; Goanta, A.; Spliethoff, H. Numerical investigation of influence of homogeneous/heterogeneous ignition/combustion mechanisms on ignition point position during pulverized coal combustion in oxygen enriched and recycled flue gases atmosphere. *Int. J. Heat Mass Transf.* **2011**, *54*, 921–931.
12. Toporov, D.; Bocian, P.; Heil, P.; Kellermann, A.; Stadler, H.; Tschunko, S.; Foerster, M.; Kneer, R. Detailed investigation of a pulverized fuel swirl flame in CO_2/O_2 atmosphere. *Combust. Flame* **2008**, *155*, 605–618.
13. Fortunato, B.; Camporeale, S.M.; Torresi, M. A gas-steam combined cycle powered by Syngas derived from biomass. *Procedia Comput. Sci.* **2013**, *19*, 736–745.
14. Fortunato, B.; Camporeale, S.M.; Torresi, M.; Fornarelli, F.; Brunetti, G.; Pantaleo, A. A combined power plant fueled by syngas produced in a downdraft gasifier. In Proceedings of the ASME Turbo Expo, Seoul, Korea, 13–17 June 2016.
15. Khan, M.M.; Mmbaga, J.P.; Shirazi, A.S.; Trivedi, J.; Liu, Q.; Gupta, R. Modelling underground coal gasification—A review. *Energies* **2015**, *8*, 12331.
16. Aziz, M.; Budianto, D.; Oda, T. Computational fluid dynamic analysis of co-firing of palm kernel shell and coal. *Energies* **2016**, *9*, 137.
17. Xu, W.; Niu, Y.; Tan, H.; Wang, D.; Du, W.; Hui, S. A new agro/forestry residues co-firing model in a large pulverized coal furnace: Technical and economic assessments. *Energies* **2013**, *6*, 4377.
18. Bhuiyan, A.A.; Naser, J. CFD modelling of co-firing of biomass with coal under oxy-fuel combustion in a large scale power plant. *Fuel* **2015**, *159*, 150–168.
19. Le Bris, T.; Cadavid, F.; Caillat, S.; Pietrzyk, S.; Blondin, J.; Baudoin, B. Coal combustion modelling of large power plant, for NO_x abatement. *Fuel* **2007**, *86*, 2213–2220.
20. Niu, Y.; Liu, X.; Zhu, Y.; Tan, H.; Wang, X. Combustion characteristics of a four-wall tangential firing pulverized coal furnace. *Appl. Therm. Eng.* **2015**, *90*, 471–477.
21. Yin, C.; Yan, J. Oxy-fuel combustion of pulverized fuels: Combustion fundamentals and modeling. *Appl. Energy* **2016**, *162*, 742–762.
22. Rebola, A.; Azevedo, J.L. Modelling pulverized coal combustion using air and recirculated flue gas as oxidant. *Appl. Therm. Eng.* **2015**, *83*, 1–7.
23. Asotani, T.; Yamashita, T.; Tominaga, H.; Uesugi, Y.; Itaya, Y.; Mori, S. Prediction of ignition behavior in a tangentially fired pulverized coal boiler using CFD. *Fuel* **2008**, *87*, 482–490.
24. Tan, H.; Niu, Y.; Wang, X.; Xu, T.; Hui, S. Study of optimal pulverized coal concentration in a four-wall tangentially fired furnace. *Appl. Energy* **2011**, *88*, 1164–1168.
25. McConnell, J.; Goshayeshi, B.; Sutherland, J.C. An evaluation of the efficacy of various coal combustion models for predicting char burnout. *Fuel* **2016**, doi:10.1016/j.fuel.2016.11.052.
26. McConnell, J.; Sutherland, J.C. The effect of model fidelity on prediction of char burnout for single-particle coal combustion. In Proceedings of the Combustion Institute, Seattle, WA, USA, 21–22 March 2016.
27. Goshayeshi, B.; Sutherland, J.C. A comparison of various models in predicting ignition delay in single-particle coal combustion. *Combust. Flame* **2014**, *161*, 1900–1910.
28. Tu, Y.; Liu, H.; Su, K.; Chen, S.; Liu, Z.; Zheng, C.; Li, W. Numerical study of H_2O addition effects on pulverized coal oxy-MILD combustion. *Fuel Process. Technol.* **2015**, *138*, 252–262.
29. Zhou, H.; Huang, Y.; Mo, G.; Liao, Z.; Cen, K. Conversion of fuel-N to N_2O and NO_x during coal combustion in combustors of different scale. *Chin. J. Chem.Eng.* **2013**, *21*, 999–1006.
30. Han, D.S.; Kim, G.B.; Kim, H.S.; Jeon, C.H. Experimental study of NO_x correlation for fuel staged combustion using lab-scale gas turbine combustor at high pressure. *Exp. Therm. Fluid Sci.* **2014**, *58*, 62–69.

31. Liu, G.; Chen, Z.; Li, Z.; Li, G.; Zong, Q. Numerical simulations of flow, combustion characteristics, and NO_x emission for down-fired boiler with different arch-supplied over-fire air ratios. *Appl. Therm. Eng.* **2014**, *75*, 1034–1045.
32. Dal Secco, S.; Juan, O.; Louis-Louisy, M.; Lucas, J.Y.; Plion, P.; Porcheron, L. Using a genetic algorithm and CFD to identify low NO_x configurations in an industrial boiler. *Fuel* **2015**, *158*, 672–683.
33. Park, H.Y.; Baek, S.H.; Kim, Y.J.; Kim, T.H.; Kang, D.S.; Kim, D.W. Numerical and experimental investigations on the gas temperature deviation in a large scale, advanced low NO_x, tangentially fired pulverized coal boiler. *Fuel* **2013**, *104*, 641–646.
34. Jeong, H.J.; Seo, D.K.; Hwang, J. CFD modeling for coal size effect on coal gasification in a two-stage commercial entrained-bed gasifier with an improved char gasification model. *Appl. Energy* **2014**, *123*, 29–36.
35. Wen, X.; Jin, H.; Stein, O.T.; Fan, J.; Luo, K. Large Eddy Simulation of piloted pulverized coal combustion using the velocity-scalar joint filtered density function model. *Fuel* **2015**, *158*, 494–502.
36. Warzecha, P.; Boguslawski, A. LES and RANS modeling of pulverized coal combustion in swirl burner for air and oxy-combustion technologies. *Energy* **2014**, *66*, 732–743.
37. Mazzitelli, I.M.; Fornarelli, F.; Lanotte, A.S.; Oresta, P. Pair and multi-particle dispersion in numerical simulations of convective boundary layer turbulence. *Phys. Fluids* **2014**, *26*, 055110.
38. Tabet, F.; Gokalp, I. Review on CFD based models for co-firing coal and biomass. *Renew. Sustain. Energy Rev.* **2015**, *51*, 1101–1114.
39. Black, S.; Szuhánszki, J.; Pranzitelli, A.; Ma, L.; Stanger, P.; Ingham, D.; Pourkashanian, M. Effects of firing coal and biomass under oxy-fuel conditions in a power plant boiler using CFD modelling. *Fuel* **2013**, *113*, 780–786.
40. Gubba, S.; Ingham, D.; Larsen, K.; Ma, L.; Pourkashanian, M.; Tan, H.; Williams, A.; Zhou, H. Numerical modelling of the co-firing of pulverised coal and straw in a 300 MWe tangentially fired boiler. *Fuel Process. Technol.* **2012**, *104*, 181–188.
41. Saha, M.; Chinnici, A.; Dally, B.B.; Medwell, P.R. Numerical study of pulverized coal MILD combustion in a self-recuperative furnace. *Energy Fuels* **2015**, *29*, 7650–7669.
42. Kong, X.; Zhong, W.; Du, W.; Qian, F. Compartment modeling of coal gasification in an entrained flow gasifier: A study on the influence of operating conditions. *Energy Convers. Manag.* **2014**, *82*, 202–211.
43. Torresi, M.; Fortunato, B.; Camporeale, S.M.; Saponaro, A. CFD modeling of pulverized coal combustion in an industrial burner. In Proceedings of the ASME Turbo Expo, Copenhagen, Denmark, 11–15 June 2012.
44. Bireswar, P.; Amitava, D. Burner development for the reduction of NO_x emissions from coal fired electric utilities. *Recent Pat. Mech. Eng.* **2008**, *1*, 175–189.
45. Patankar, S. *Numerical Heat Transfer and Fluid Flow*; Hemisphere: Washington, DC, USA, 1980.
46. Shih, T.H.; Liou, W.; Shabbir, A.; Yang, Z.; Zhu, J. A new k-ϵ eddy-viscosity model for high Reynolds number turbulent flows—Model development and validation. *Comput. Fluids* **1995**, *24*, 227–238.
47. *FLUENT: User's Guide 6.3*; Fluent Inc.: Lebanon, NH, USA, 2006.
48. Siegel, R.; Howell, J.R. *Thermal Radiation Heat Transfer*; Hemisphere Publishing Corporation: Washington, DC, USA, 1992.
49. Sazhin, S.; Sazhina, E.; Faltsi-Saravelou, O.; Wild, P. The P-1 model for thermal radiation transfer: Advantages and limitations. *Fuel* **1996**, *75*, 289–294.
50. Horsfall, D. A general review of coal preparation in South African. *J. S. Afr. Inst. Min. Metall.* **1980**, *80*, 257–268.
51. Torresi, M.; Camporeale, S.M.; Fortunato, B.; Ranaldo, S.; Mincuzzi, M.; Saponaro, A. Diluted combustion in a aerodynamically staged swirled burner fueled by Diesel oil. In Proceedings of the Conference on Processes and Technologies for a Sustainable Energy, Ischia, Italy, 27–30 June 2010.
52. Badzioch, T.; Hawksley, P. Kinetics of thermal decomposition of pulverized coal particles. *Ind. Eng. Chem. Process Des. Dev.* **1970**, *9*, 521–530.
53. Williams, A.; Backreedy, R.; Habib, R.; Jones, J.; Pourkashanian, M. Modelling coal combustion: The current position. *Fuel* **2002**, *81*, 605–618.
54. Fletcher, T.H.; Kerstein, A.R.; Pugmire, R.J.; Grant, D.M. Chemical percolation model for devolatilization: 2. Temperature and heating rate effects on product yields. *Energy Fuels* **1990**, *4*, 54–60.
55. Fletcher, T.H.; Kerstein, A.R.; Pugmire, R.J.; Solum, M.S.; Grant, D.M. Chemical percolation model for devolatilization. 3. Direct use of ^{13}C NMR data to predict effects of coal type. *Energy Fuels* **1992**, *6*, 414–431.

56. Van Niekerk, D.; Pugmire, R.J.; Solum, M.S.; Painter, P.C.; Mathews, J.P. Structural characterization of vitrinite-rich and inertinite-rich Permian-aged South African bituminous coals. *Int. J. Coal Geol.* **2008**, *76*, 290–300.
57. Grant, D.M.; Pugmire, R.J.; Fletcher, T.H.; Kerstein, A.R. Chemical percolation model of coal devolatilization using percolation lattice statistics. *Energy Fuels* **1989**, *3*, 175–186.
58. Cloke, M.; Lester, E.; Thompson, A. Combustion characteristic of coals using drop tube furnace. *Fuel* **2002**, *81*, 727–735.
59. Wu, T.; Lester, E.; Cloke, M. A burnout prediction model based around char morphology. *Energy Fuels* **2006**, *20*, 1175–1183.
60. Van Niekerk, D.; Mitchell, G.; Mathews, J. Petrographic and reflectance analysis of solvent-swelled and solvent-extracted South African vitrinite-rich and inertinite-rich coals. *Int. J. Coal Geol.* **2010**, *81*, 45–52.
61. Baum, M.; Street, P. Predicting the Combustion Behavior of Coal Particles. *Combust. Sci. Technol.* **1971**, *3*, 231–243.
62. Field, M. Rate of combustion of size-graded fractions of char from a low rank coal between 1200 K–2000 K. *Combust. Flame* **1969**, *13*, 237–252.
63. Haas, J.; Tamura, M.; Weber, R. Characterization of coal blends for pulverized coal combustion. *Fuel* **2001**, *80*, 1317–1323.
64. Smith, I. The intrinsic reactivity of carbons to oxygen. *Fuel* **1978**, *57*, 409–414.
65. Laurendeau, N. Heterogeneous kinetics of coal char gasification and combustion. *Prog. Energy Comb. Sci.* **1978**, *4*, 221–270.
66. Smith, I. The Combustion Rates of Coal Chars: A review. In Proceedings of the 19th International Symposium on Combustion, Orlando, FL, USA, 10–12 May 1982; pp. 1045–1065.
67. Hanson, R.; Salimian, S. *Survey of Rate Constants in H/N/O Systems*; Gardiner, W.C., Jr., Ed.; Springer: New York, NY, USA, 1984.
68. Soete, G.D. Overall Reaction Rates of NO and N_2 Formation from Fuel Nitrogen. In Proceedings of the 15th International Symposium on Combustion, Tokyo, Japan, 25–31 August 1975; pp. 1093–1102.